Nuclear Inst. and Methods in Physics Research, A 1034 (2022) 166783

Contents lists available at ScienceDirect

Nuclear Inst. and Methods in Physics Research, A

journal homepage: www.elsevier.com/locate/nima

A study of the feasibility of coded aperture imaging technique for elemental analysis by muonic X-ray measurements based on Geant4 simulations

Zebin Lin[1], Ziwen Pan [*,1], Zhe Wang, Zhengyang He, Jingyu Dong, Jiandang Liu, Hongjun Zhang, Bangjiao Ye [*]

State Key Laboratory of Particle Detection and Electronics, University of Science and Technology of China, Hefei 230026, China

ARTICLE INFO

Keywords:
Muonic X-ray imaging
Coded aperture imaging
Pinhole imaging
Figure of merit

ABSTRACT

A novel method of muonic X-ray imaging based on the coded aperture imaging technique is developed. The image quality and detection rate of X-rays can be influenced by the number of detected counts (N_D), mask size (thickness t and aperture size d) and sample-to-detector distance (D_{SD}). A figure of merit (FoM) is introduced as an integral and quantitative indicator of these influences. The choice of optimal values of the parameters N_D, t, d and D_{SD} is achieved therefore by the comparison of respective FoM values. As compared to the conventional pinhole imaging technique, the coded aperture technique provides slightly better image quality and has a two orders of magnitude higher detection rate. Therefore, the FoM value for the coded aperture imaging technique is higher than that for the pinhole one by a factor not smaller than 1.67. Obtained results demonstrate that the coded aperture imaging technique has significant advantages for the applications for elemental analysis by muonic X-ray measurements.

1. Introduction

Muonic X-ray Emission Spectroscopy (μ-XES) is a quantitative technique for elemental analysis intended to identify both the concentrations and chemical states of elements [1]. Muonic X-rays are generated by de-excitation of muonic atoms which are formed by the capture of negative muons (μ^-) in the Coulomb field of nuclei. Due to the large mass of negative muons (207 times higher than the electron mass), muonic X-rays are emitted with relatively high energies (0.2–6 MeV) as compared to the energy of electronic X-rays [2]. Therefore, muonic X-rays can easily leave bulk samples without significant photon self-absorption. Consequently, the elemental composition of samples, especially those containing atoms with low atomic numbers, can be identified using a semiconductor detector with high-energy resolution [3]. Since the momentum of a negative muon beam is tunable, the depth-dependent elemental distribution in a sample can also be extracted. μ-XES was successfully applied for research of archaeological objects [4], in bioscience [5], for probing extraterrestrial materials [6], investigations of lithium batteries [7] and a number of other applications [1,2,8].

Spatial distribution of elements obtained by μ-XES can be imaged by pixelated detectors. For example, Hillier placed a pixelated CdTe detector at a distance of 4 mm behind the sample at ISIS (High Energy X-ray Imaging Technology, HEXITEC) [9]. The sample comprised a 4-mm thick graphite block, a 3-mm thick aluminum block and a 3-mm thick magnetite block. The possibility of imaging element distribution in this sample with the HEXITEC detector was confirmed by the proximity images of each block. The image quality was limited by the solid angle covered by the HEXITEC detector and the high intensity of background scattering events. Katsuragawa developed an imaging system based on a CdTe doubled-sided strip detector to get the 3D distribution of low-Z elements (B, N and F) at J-PARC [10]. A pinhole between the sample and the detector was used to collimate X-rays, so that image reconstruction artifacts could be effectively avoided. Due to the low detection rate of such experimental setup, one image required 20 h of muon exposure. The system could make an image of a small block with a size over 5×5 mm^2.

An Experimental Muon Source (EMuS) is proposed to install at the China Spallation Neutron Source (CSNS). About 5% of the proton beam power (1.6 GeV, 25 Hz, 500 kW) will be allocated to EMuS to produce muons. Relatively low repetition rate as compared to that at ISIS (40 Hz) [11] and J-PARC (25 Hz) [12] will largely limit the counting rate in future μ-XES applications at EMuS. Analogously to the muonic X-ray imaging experiments conducted at the J-PARC, a single pinhole will be replaced by a coded mask (multiple pinholes), which will lead to a significant increase of the counting rate at the same time maintaining the image quality. The coded aperture imaging technique combined with use of X- and γ-rays is widely applied in various research fields including astrophysics [13], medical physics [14], nuclear safety [15]

* Corresponding authors.
E-mail addresses: panzw19@ustc.edu.cn (Z. Pan), bjye@ustc.edu.cn (B. Ye).
[1] These authors contributed equally to this work.

https://doi.org/10.1016/j.nima.2022.166783
Received 13 December 2021; Received in revised form 14 April 2022; Accepted 15 April 2022
Available online 4 May 2022

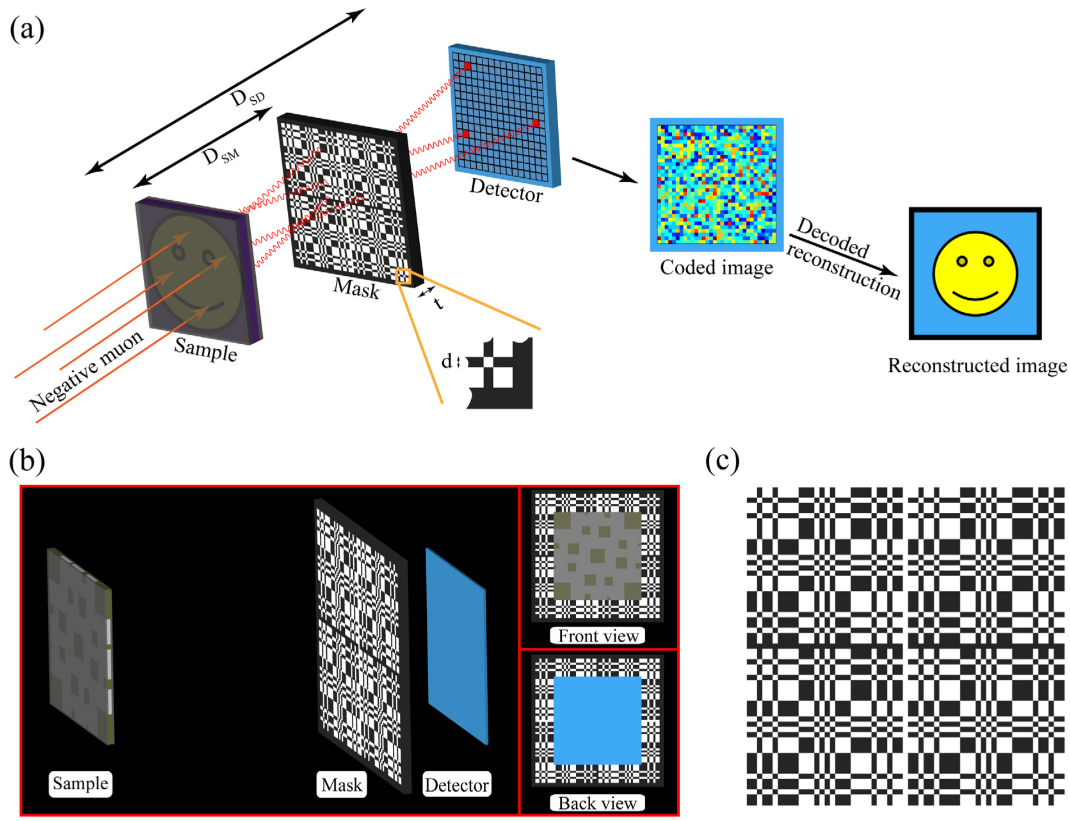

Fig. 1. (a) Illustration of coded imaging and decoded reconstruction in the coded aperture imaging technique. D_{SM} is the distance between the sample and the mask, D_{SD} is the distance between the sample and the pixelated detector, t is the thickness of the mask, and d is the size of an aperture on the mask, (b) geometric structure of the simulation setup in Geant4, (c) pattern of the mask used in the simulation.

and X-ray fluorescent analysis [16]. In the present work, the feasibility of this technique for μ-XES is thoroughly studied based on Geant4 [17–19] simulations. The image quality can be affected by the imaging technique, the number of detected counts, the size of coded mask, and the relative positions of sample, mask and detector. The impacts of all these influencing factors are quantitatively estimated and the factors themselves are optimized aimed at the application of the code aperture imaging technique in the EMuS imaging detection system at the CSNS.

2. Principle of coded aperture imaging and simulation method

2.1. Principle of coded aperture imaging

The coded aperture imaging technique includes two main steps, which are illustrated in Fig. 1(a), namely coded imaging and decoded reconstruction. In the first step, a coded mask is placed between an object and a pixelated detector such as e.g. a CdTe one. The image I detected by the latter can be considered as a convolution of the object function O and the mask function A, which can be expressed as follows:

$$I \simeq O * A + N, \tag{1}$$

where asterisk denotes the convolution operator and N is the signal-independent noise, respectively [20,21]. Transparent or opaque pixels on the mask can be expressed by the following function:

$$A(i,j) = \begin{cases} 1, & \text{transparent} \\ 0, & \text{opaque,} \end{cases} \tag{2}$$

where i and j denote the order of a pixel along the horizontal and the vertical axis, respectively. Thereafter, the detected image can be reconstructed by

$$\hat{O} = I \otimes G \simeq (O * A + N) \otimes G \simeq O, \tag{3}$$

$$G(i,j) = \begin{cases} 1, & A(i,j) = 1 \\ -1, & A(i,j) = 0, \end{cases} \tag{4}$$

where $\hat{O}$ is the reconstructed object, $\otimes$ is the cross-correlation operator, and G is a 2D array, respectively.

Current reconstruction methods [22,23] of coded aperture imaging include deconvolution (Fast Fourier Transform, FFT), iterative algorithm (Maximum-Likelihood Expectation Maximization, MLEM [24,25]), convolutional neural network [22,26] and correlation analysis. The FFT deconvolution method needs to determine the filter function according to the imaging mode to reduce the noise. The iterative algorithm method such as MLEM can effectively reduce noise, while the reconstruction is time-consuming and requires high computing performance. Convolutional neural network is a new reconstruction method, which can significantly improve the quality of images, but it needs a large number of imaging samples as training before reconstruction. The methods mentioned above are mainly based on the reduction of noise. In addition, an increase of detection counts can also help improve the image quality such as the correlation analysis. Compared with other methods, the reconstruction processes of correlation analysis are simple and easy to be implemented. In this work, a correlation analysis using finely sampled balanced correlation [27] was employed for image reconstruction.

2.2. Geant4 simulation model

The imaging process was modeled using the Geant4 10.5 software and reconstructed by a standalone code. The geometry of the imaging system in Geant4 was shown in Fig. 1(b). The physical list, QBBC, was chosen to simulate the capture of negative muons by nuclei, emission of muonic X-rays, muon decays and respective electromagnetic interactions. Table 1 lists main parameters related to the negative muon beam,

Table 1
Parameters of negative muon beam, coded mask and CdTe detector used in Geant4 simulations.

Object	Parameter	Value
Muon beam	Momentum dispersion (%)	5
	Size of beam spot (mm^2)	32 × 32
	Spatial distribution of beam spot corresponding to the Full Width at Half Maximum (FWHM) (mm^2)	70 × 60
Sample	Dimensions (mm^3)	31 × 31 × 2
Coded mask	MURA array	61 × 61
	Material	Pb
	Thickness t (mm)	0.5–4.0
	Aperture size d (mm)	0.65–0.95
Detector	Pixel array	128 × 128
	Cell size (mm^3)	0.25 × 0.25 × 0.75
	Area(mm^2)	32 × 32
	Detector readout	Photon energy and hit position
	Energy resolution (%)	1.06 [31]
Distance	D_{SD} (mm)	20–240
	D_{SM} to D_{SD} ratio	0.75

sample, coded mask, and CdTe detector [28,29] shown in Fig. 1(a). The detector was required to record the energy and hit position of each photon. The position of photons discriminated by energy was used to reconstruct the sample image. Fig. 1(c) shows the mosaic of two cycles of rank 31 MURA mask [30] used in the simulation. The thickness t and the aperture size d of the coded mask varied in steps of 0.5 and 0.1 mm, respectively, to study their impacts on image quality. The sample had a three-layer "sandwich" structure, which is shown in Fig. 2. The central layer consisted of several carbon blocks inserted in an aluminum plate, while the top and the bottom layers were pure aluminum. To simplify the calculations, the ratio of sample-to-mask distance to sample-to-detector distance D_{SM}/D_{SD} was fixed.

2.3. Quality evaluation of coded aperture imaging

The quality of image reconstruction can be evaluated using a universal image quality index, Q, which is defined as follows [32]:

$$Q = \frac{2\mathrm{cov}(O,\hat{O})}{\mathrm{var}(O)+\mathrm{var}(\hat{O})}\,\frac{2\bar{O}\cdot\bar{\hat{O}}}{\bar{O}^2+\bar{\hat{O}}^2}, \tag{5}$$

where "cov" and "var" correspond to the covariance and variance function, respectively, O is the image of a sample, and $\hat{O}$ is the reconstructed image, respectively, $\bar{O}$ and $\bar{\hat{O}}$ are the average values of O and $\hat{O}$, respectively. According to Eq. (5), the parameter Q varies in the range of $[-1, 1]$. A high quality of reconstructed image is indicated by the values of Q close to 1.

The detection rate of X-rays is another important variable, which determines the measurement time needed to achieve the required precision. The detection rate ε can be expressed as follows:

$$\varepsilon = \frac{N_D}{N_{Tot}} \tag{6}$$

where N_D is the total number of detected X-rays that energy in the energy window and N_{Tot} is the total number of primary negative muons, respectively. The value of this parameter mainly depends on the covered solid angle of a detector in the sample coordinate and the transparency of a coded mask.

3. Momentum setting and energy window selection

We simulated the implantation profiles of muons to confirm that most of them can stop inside the carbon layer of the sandwiched sample. As shown in Fig. 3(a), the peak position of a muon distribution shifts deep in the sample with the increase of muon kinetic energy. The red plot in Fig. 3(b) presents the dependence of the fraction of negative muons stopping inside the second layer (C layer consists of carbon blocks and aluminum blocks) on their kinetic energy. As can be seen from this figure, nearly 100% of these muons with the energies in the range of 4.4–5.1 MeV stop in the second layer. Therefore, the momentum of negative muons was set to 32.89 MeV/c (i.e. corresponding to the energy of 5 MeV) with a dispersion of 5% for Geant4 simulations. In the simulation, muons are deposited inside the sample, so that background events outside the sample are limited to zero. As only several carbon blocks were inserted in the aluminum plate, the highest fraction of negative muons stopped inside these blocks was around 0.24, as the black plot in Fig. 3(b). In order to obtain only the contributions from carbon elements, the energy windows of ±1.5 keV each were set around the characteristic energies of 72.55 and 13.85 keV corresponding to the μC-K$_\alpha$ and μC-L$_\alpha$ lines, respectively, as the red line shown in Fig. 3(c).

4. Performance of imaging system under different conditions

4.1. Impact of detected counts and position of CdTe detector

The anti-mask technique was developed for coded aperture imaging measurements to reduce second-order artifacts as compared to the conventional only-mask technique [33]. In this technique, 50% of the total number of negative muons are simulated using the mask, and simulation of the remaining counts takes place with the anti-mask obtained by rotating the mask by 90° [34]. According to Eq. (2), the function of anti-mask, A', is defined as

$$A' = 1 - A, \tag{7}$$

then the image I' recorded by detector is defined as a convolution of object O and the anti-mask A'

$$I' \simeq O * A' + N', \tag{8}$$

where N' is noise. According to Eqs. (3), (4), the reconstructed image $\hat{O}'$ is

$$\hat{O}' = I' \otimes G \simeq (O - O * A + N) \otimes G = O \otimes G - O + N' \otimes G. \tag{9}$$

The image reconstructed by the anti-mask technique can be derived by

$$\hat{O} - \hat{O}' \simeq 2O + (N - N') \otimes G. \tag{10}$$

The usage of anti-mask technique can reduce the noise by the operation $(N - N') \otimes G$.

Fig. 4(a–f) shows the reconstructed images obtained using the only-mask and the anti-mask techniques at different values of D_{SD} for given $d = 0.75$ mm and $t = 2.0$ mm. As can be seen from this figure, the images reconstructed using the anti-mask technique contain less second-order artifacts (the artifacts of the edge of panels (a–c)) [33,34]. As shown in panels (d–f), the anti-mask technique enables to obtain more distinct contours of carbon blocks at medium D_{SD} values (D_{SD} = 50 mm). This is because the anti-mask technique can suppress noise according to Eq. (10). The images reconstructed using anti-mask technique at different number of detected counts for given $D_{SD} = 50$ mm, $d = 0.75$ mm

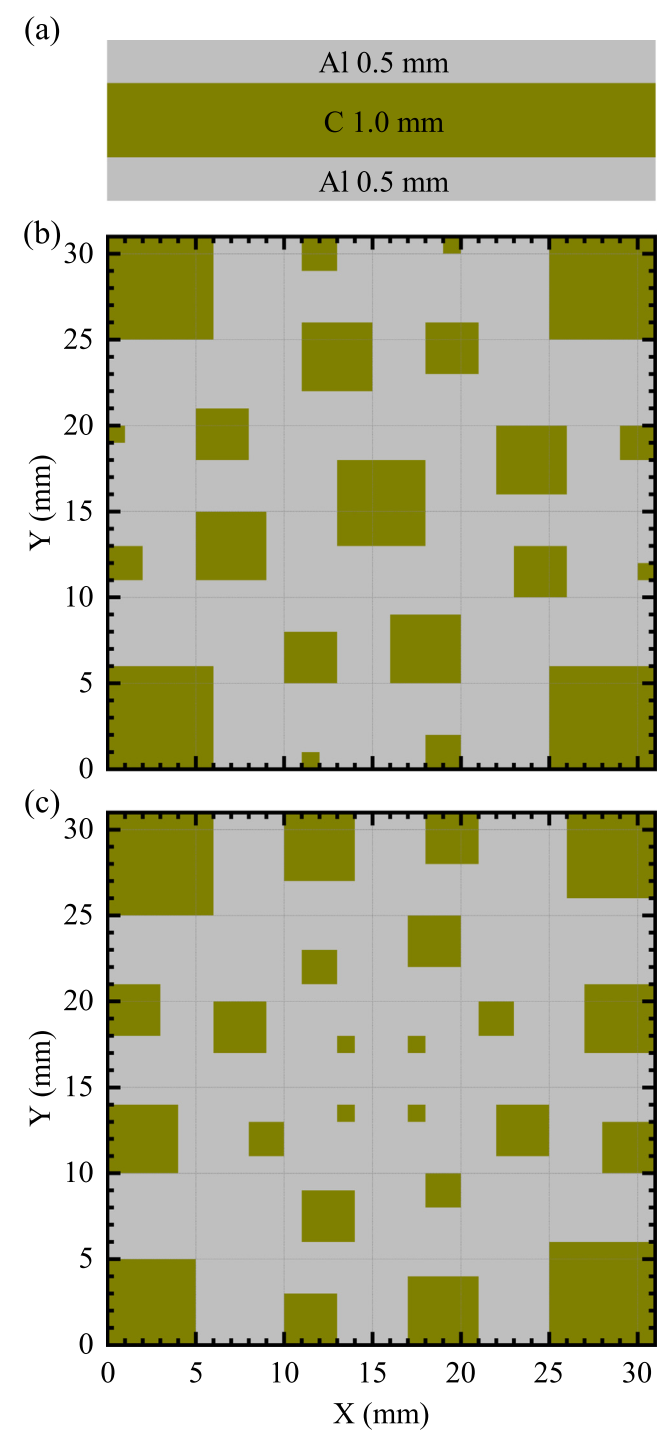

Fig. 2. (a) Sandwich structure of the sample, and (b, c) the second layer containing several carbon blocks (yellow) inserted in an aluminum plate (gray). The sizes of carbon blocks range from 1 to 6 mm. Panels (b, c) show different arrangements of blocks used to investigate the dependence of image quality on the edge block size.

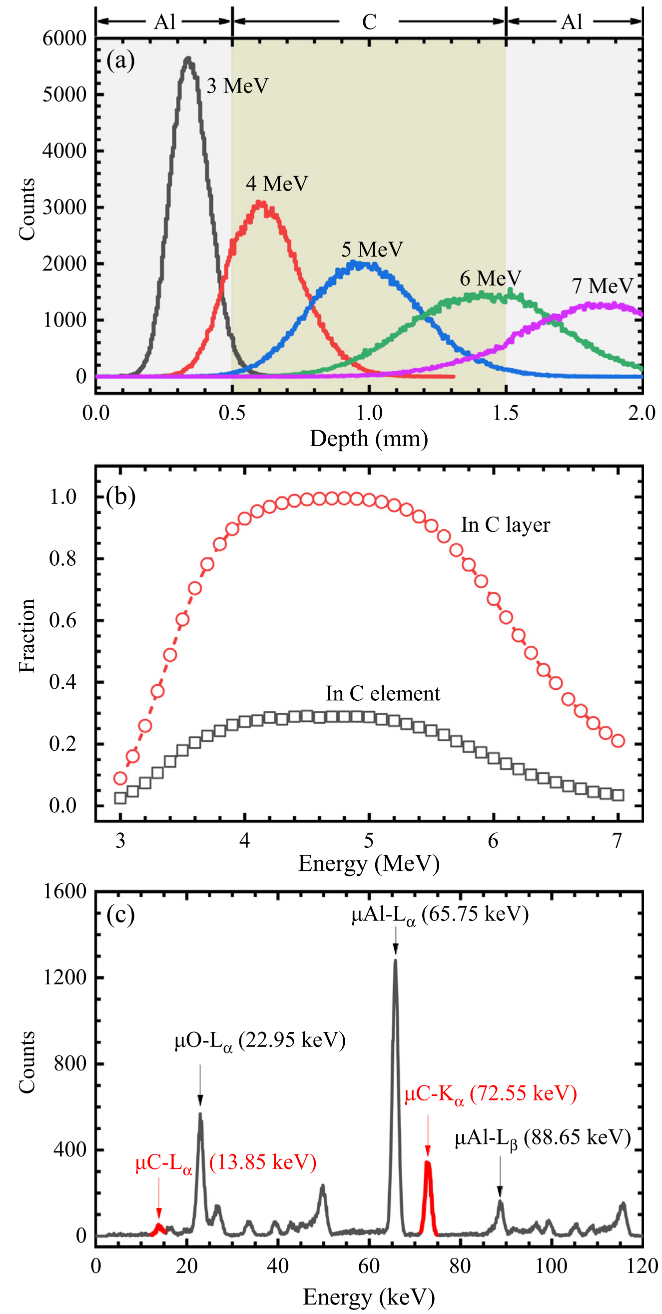

Fig. 3. (a) Depth distribution of muons with different kinetic energies in the sandwiched sample, (b) fraction of negative muons that stop in the second layer (C layer consists of carbon blocks and aluminum blocks) (red) and carbon blocks (black), and (c) energy spectrum recorded by a CdTe detector.

and t = 2 mm are plotted in Fig. 5. With the increase of detection counts, the carbon blocks in the reconstructed image become clearer and the artifacts are much less. Improvement of the quality of images obtained using the coded aperture imaging technique was quantitatively confirmed by calculation of the image quality Q. Fig. 6(a) shows the image quality for the only-mask and the anti-mask techniques as a function of the number of detected counts N_D at different D_{SD} when d = 0.75 mm and t = 2 mm. The data obtained for both techniques show a rising trend with saturation after several hundred thousand counts. By averaging Q values that N_D higher than 1.5×10^5 at different D_{SD} with d = 0.75 mm and t = 2 mm, the dependences presented in Fig. 6(b) are obtained clearly demonstrating better image quality provided by using the anti-mask technique as compared to that obtained with the only-mask technique. Therefore, the former was selected for optimization of coded aperture based muonic X-ray imaging.

Fig. 4(d–f) and Fig. 5 show the reconstructed images obtained using the anti-mask technique at different values of D_{SD} and N_D. As mentioned above, the images obtained at medium D_{SD} values have better quality as shown in Fig. 4(d–f). Regarding the influence of parameter N_D, one may notice that raising the number of detected counts can help improve the image quality. Therefore, it is necessary to find the smallest N_D while maintaining the image quality. The impacts of D_{SD} and N_D

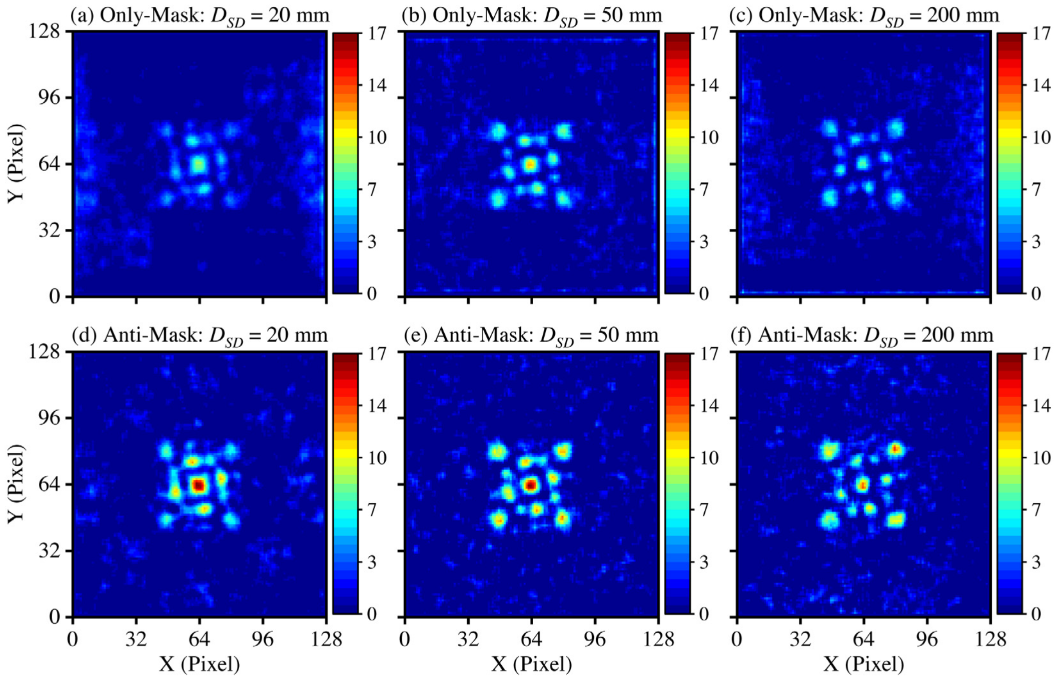

Fig. 4. The images reconstructed using the only-mask (a–c) and the anti-mask (d–f) techniques at different values of D_{SD} and the number of detected counts of 1.5×10^5. In all the plots, the dimensions of the mask d and t are set to 0.75 and 2.0 mm, respectively.

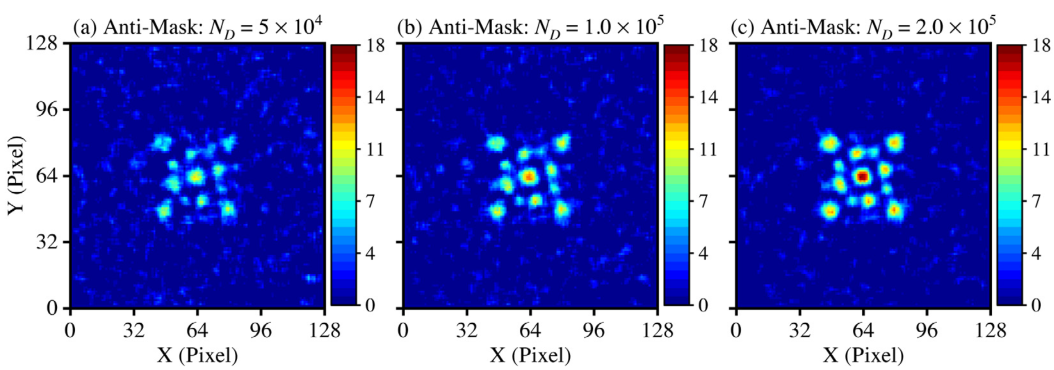

Fig. 5. The images reconstructed using the anti-mask technique at different numbers of detected counts and D_{SD} = 50 mm. In all the plots, the dimensions of the mask d and t are set to 0.75 and 2.0 mm, respectively.

on image quality were quantitatively estimated. Fig. 7(a) and (b) show similar saturation trends for these characteristics plotted as functions of N_D and D_{SD}. The data points presented in these two panels can be fitted by the following dependences:

$$Q = Q_0 + Q_1 e^{-\frac{N_D}{\lambda_N}}, \tag{11}$$

$$Q = Q_0 + Q_1 e^{-\frac{D_{SD}}{\lambda_D}}, \tag{12}$$

where Q_0, Q_1, λ_N and λ_D are the fitting parameters. The λ_N and λ_D in the exponents are the characteristic values reflecting the image quality saturation rate. Fig. 7(c, d) presents the dependences for the values of $3\lambda_N$ and $3\lambda_D$ as such a factor is large enough to ensure saturation of exponential functions in the expressions (11) and (12) and, hence, saturation of Q. i.e. Q will approach its saturation value at $N_D = 3\lambda_N$ and $D_{SD} = 3\lambda_D$. At this, the values of N_D and D_{SD} should not be smaller than 1.5×10^5 and 50 mm, respectively. Fig. 7(e) shows that the detection rate quickly decreases with the increase of D_{SD}, which is resulted from the drop of radiation intensity according to the inverse square law. To integrally evaluate the impact of N_D and D_{SD} on both Q and ε, a figure of merit (FoM) was introduced as follows:

$$FoM = \frac{Q}{|\ln \varepsilon|}. \tag{13}$$

The logarithm is introduced in Eq. (13) to balance the influences of the number of detected counts (N_D), sample-to-detector distance (D_{SD}) and mask size (thickness t and aperture size d) on Q and ε. As shown in Fig. 7(f), the FoM peaks at D_{SD} = 50 mm. At $N_D > 2.0 \times 10^5$ counts and D_{SD} = 50 mm, the value of FoM almost does not change with N_D. Therefore, the values of N_D and D_{SD} can be set to 2.0×10^5 and 50 mm, respectively.

4.2. Impact of the size of the coded mask

Fig. 8(a) shows that the image quality peaks at $t \approx 1$ mm and then gradually decreases. Such trend is similar for small aperture sizes (d = 0.65 mm, d = 0.75 mm), but with a flat from t = 0.5 mm to t = 2.5 mm at the larger aperture sizes (d = 0.85 mm, d = 0.95 mm). This is because the aperture size will affect the transmission angle of X-rays at same thickness. The detection rate presented in Fig. 8(b) also

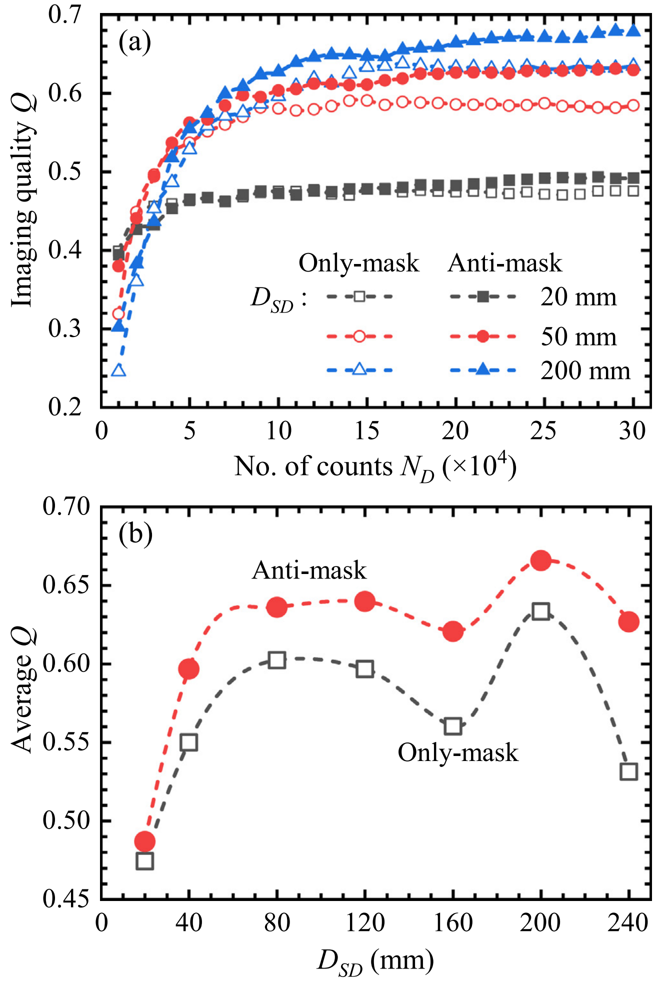

Fig. 6. (a) Quality of reconstructed images obtained using the only-mask and the anti-mask techniques at different values of N_D and D_{SD}, and (b) average image quality obtained by averaging the values of Q at N_D in the range of $(1.5\text{–}3.0)\times10^5$ counts. The parameters of the mask are $d = 0.75$ mm and $t = 2.0$ mm. Dashed curves are guides for eyes.

shows a decreasing trend with the mask thickness due to increase of the absorption and scattering of X-rays by thicker masks. In the same figure, the masks with larger apertures allow more X-rays to get to the detector, which is supported by the increase of detection rate with the aperture size. As can be further seen in Fig. 8(c), FoM obtained at different aperture sizes demonstrate a decreasing trend with the thickness of mask similar to the already considered functions. Fig. 8(d) shows the dependence of average FoM calculated by averaging FoM values for different aperture sizes, on the mask thickness. The results obtained demonstrate that the highest average FoM value is reached at the thickness of mask equal to 1 mm. Therefore, this parameter can be set to 1 mm. Under such condition, the image quality and FoM reach the highest values at the optimal aperture size equal to 0.75 mm as can be observed in panels (a) and (c) of Fig. 8.

4.3. Image quality with optimal parameters

According from simulation results described in Sections 4.1–4.2, the optimal parameters for the coded mask and the detector were found, which are listed in Table 2. Fig. 9 shows the reconstructed images simulated with these parameters. Both panels in this figure demonstrate

Table 2
Optimal parameters of the coded mask and the detector.

Parameters	Values
N_D	2.0×10^5
D_{SD} (mm)	50
D_{SM} (mm)	37.5
t (mm)	1.0
d (mm)	0.75

Table 3
Image quality, detection rate and FoM for the coded aperture and the pinhole imaging techniques. The first row corresponds to the configuration with optimal parameters listed in Table 2.

Imaging technique	D_{SD} (mm)	d (mm)	t (mm)	Q	ε	FoM
Coded aperture	50	0.75	1.0	0.677	2.37×10^{-3}	0.112
	80	0.75	1.0	0.670	1.25×10^{-3}	0.100
Pinhole	80	0.75	20.0	0.649	2.06×10^{-5}	0.060
	80	1.50	20.0	0.381	2.67×10^{-5}	0.036

that the coded aperture imaging technique is feasible to apply for μ-XES. It can be seen from Fig. 9 that the blocks with sizes not smaller than 2 mm are clearly resolved. The reconstructed images of the blocks with sizes smaller or equal to 2 mm on the edges (Fig. 9(a)) and in the center (Fig. 9(b)) are similar. For blocks with sizes over 2 mm, such "edge effect" is negligible.

4.4. Comparison of the coded aperture and the pinhole imaging techniques

Fig. 10 shows the reconstructed images obtained using the coded aperture and the pinhole imaging techniques. The thickness of a collimator with a single pinhole was set to 20 mm, and the shape of the pinhole is knife-edge with an angle about 30°. Therefore, X-rays not entering the pinhole could be effectively shielded. However, it is possible that X-rays can penetrate the thin part of the knife-edge and cause noise. The contribution of these noise was subtracted in the reconstruction process. Due to the limit imposed by the covered solid angle in the pinhole imaging technique, the distance between the detector and the sample was set to 80 mm. Comparison of the panel (a) with the panels (b, c) in Fig. 10 shows that the image of carbon blocks obtained using the coded aperture imaging technique has a higher resolution. In the pinhole imaging technique, using a narrower pinhole leads to an improvement of image quality, as can be seen in panel (b) of Fig. 10. For comparison of two imaging techniques, Table 3 lists the image quality, detection rate and FoM obtained by both of them. It can be seen from this table that the image quality achieved by the coded aperture imaging technique is slightly better than that for the pinhole one at the same values of D_{SD} and d and nearly 76% (i.e. $(0.670 - 0.381)/0.381 \times 100\%$) higher than that for the pinhole technique with $d = 1.5$ mm. The coded aperture imaging technique has an advantage that its detection rate is around two orders of magnitude that of the pinhole imaging technique. With the significant increase of the number of holes on a mask, the detection solid angle of the coded aperture imaging technique is much larger than that of the pinhole imaging technique. Evaluation of the impacts of different imaging techniques on Q and ε shows that the FoM for the coded aperture technique is higher than that for the pinhole one by a factor of at least 1.67 (i.e. 0.100/0.060). These comparisons strongly support the conclusion that the coded aperture imaging technique can be applied for μ-XES.

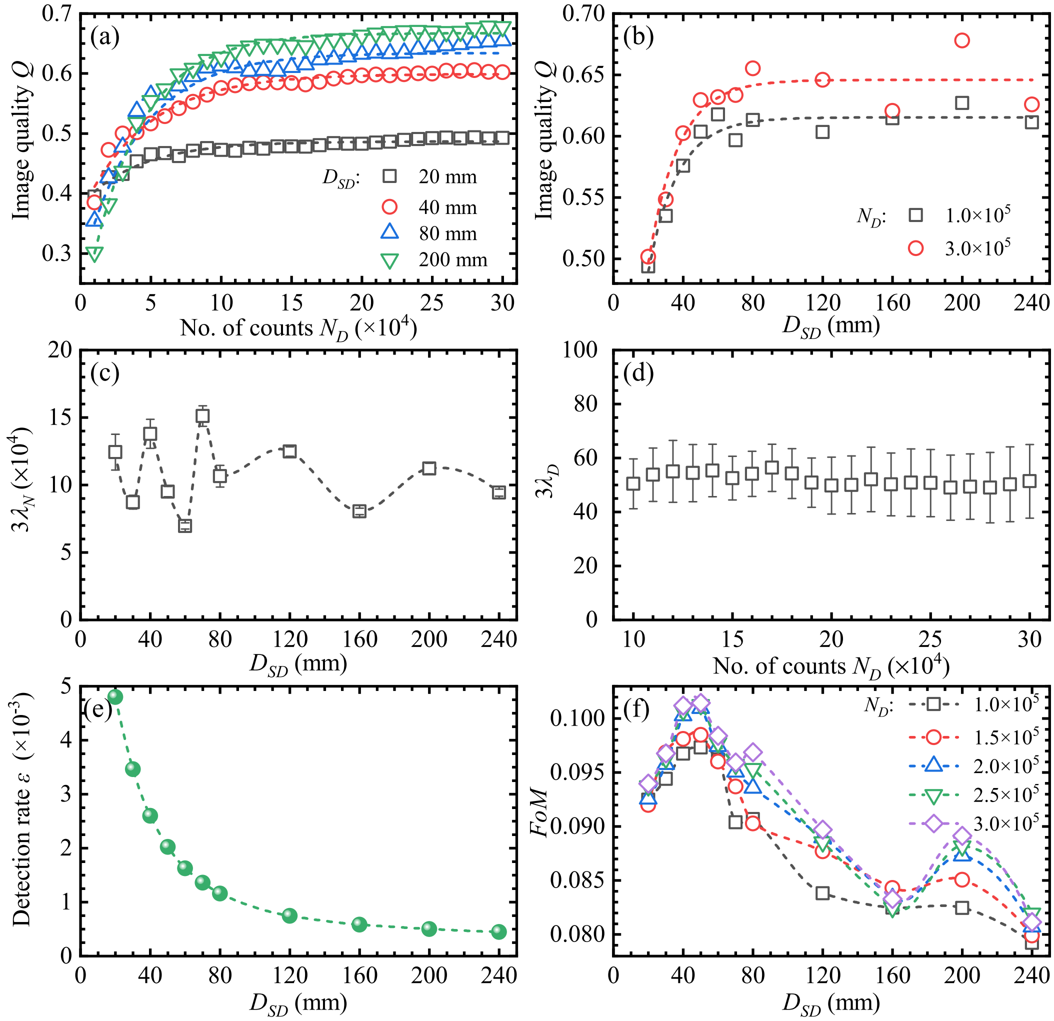

Fig. 7. (a) Image quality versus N_D, (b) image quality versus D_{SD}, (c) λ_N fitted to the data presented in panel (a), (d) λ_D fitted to the data presented in panel (b), (e) detection rate versus D_{SD}, and (f) FoM versus D_{SD} for different values of N_D. Dashed curves in (a, b) are fitted to the data points, while the ones in (c–f) are guide for eyes.

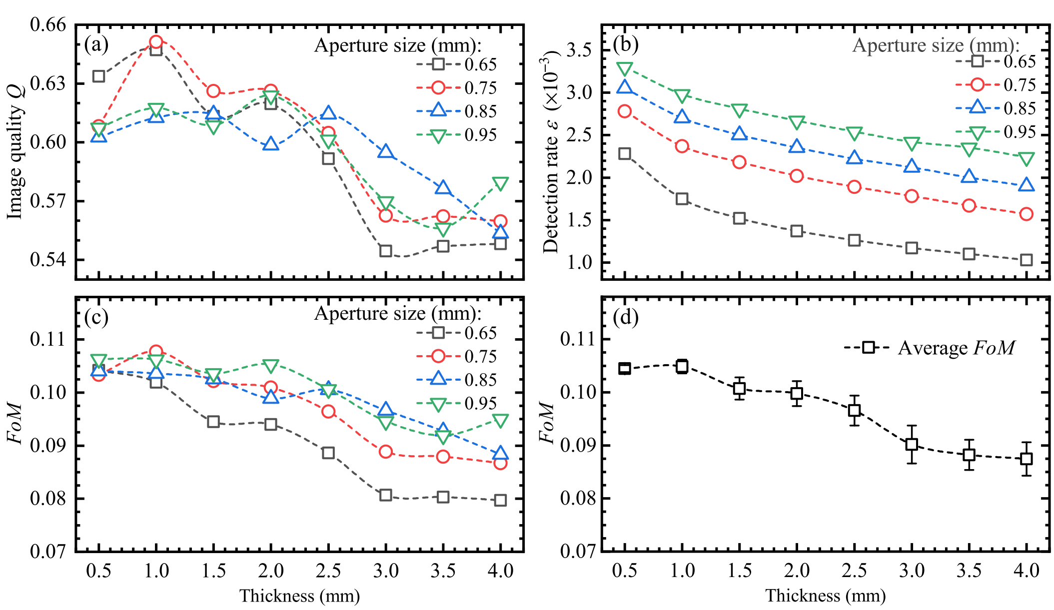

Fig. 8. (a) The image quality Q, (b) detection rate and (c) FoM as functions of the mask thickness at different aperture sizes, and (d) the average FoM values versus mask thickness. Dashed curves in all panels are guides for eyes.

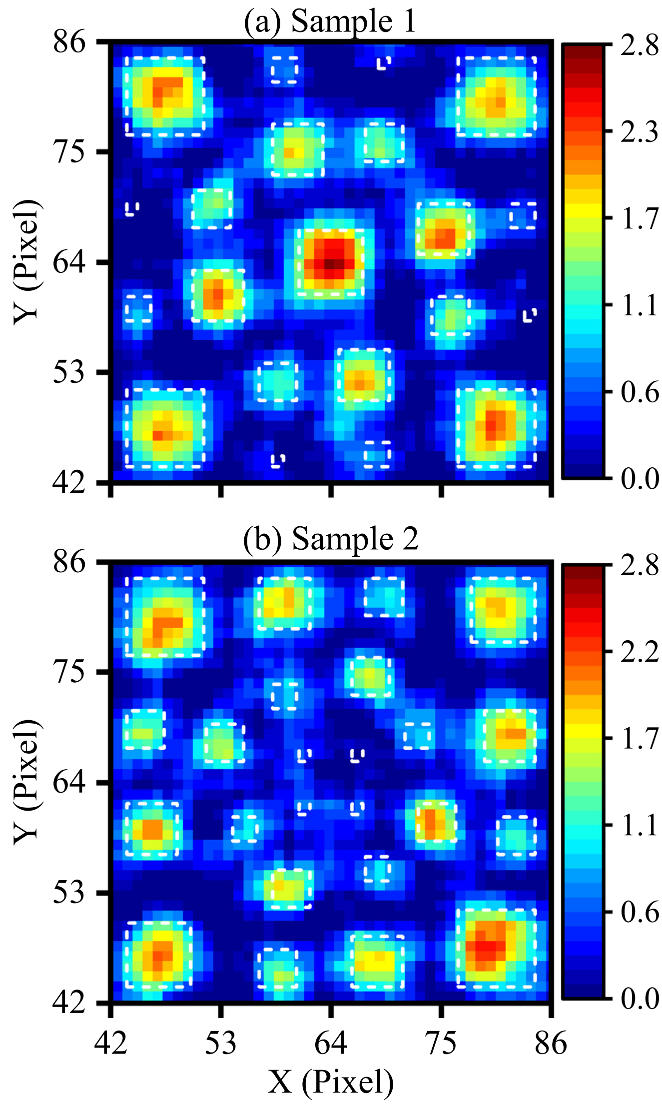

Fig. 9. Reconstructed images of the second layer of samples shown in Fig. 2(b, c) obtained at optimal parameters. White dashed squares show the positions of carbon blocks in the aluminum plate.

5. Conclusion

The feasibility of coded aperture imaging technique for μ-XES was studied using Geant4 simulations. The anti-mask technique was confirmed to result in better performance than the conventional only-mask one. A figure of merit ($Q/|\ln\varepsilon|$) was introduced to integrally and quantitatively evaluate the impacts of the number of detected counts, size of the coded mask and relative positions of the sample, mask and detector on image quality and detection rate. The optimal values of these parameters were found to be $N_D = 2.0 \times 10^5$, $t = 1.0$ mm, $d = 0.75$ mm and $D_{SD} = 50$ mm, respectively. As compared to the pinhole imaging technique, the coded aperture technique provides slightly better image quality with two orders of magnitude higher detection rate. Therefore, the coded aperture imaging technique has an advantage of the higher FoM value by a factor not less than 1.67 over the pinhole one. Our simulations confirm the suitability of the coded aperture imaging technique for applications in elemental imaging by muonic X-ray measurements.

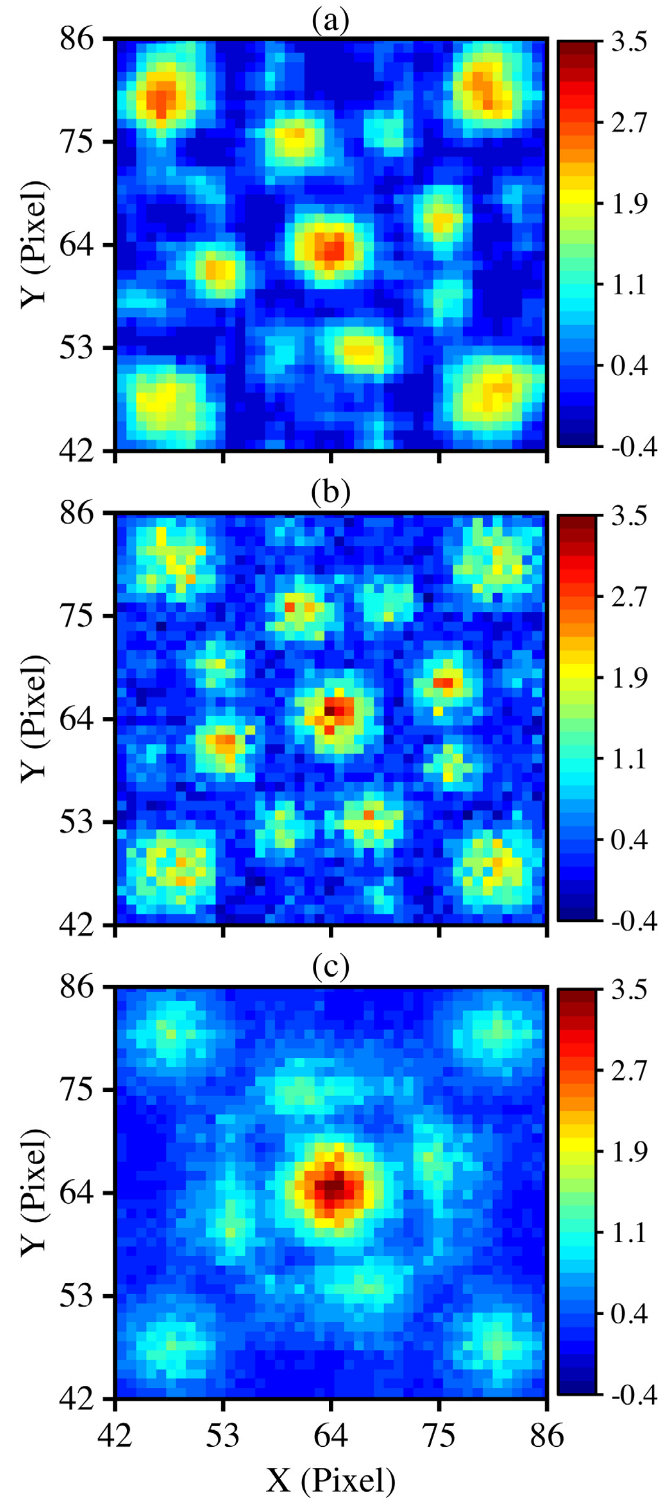

Fig. 10. Reconstructed images obtained using the coded aperture imaging technique with (a) $d = 0.75$ mm, $t = 1.0$ mm and $D_{SD} = 80$ mm, and the pinhole imaging technique with (b) $d = 0.75$ mm, $t = 20.0$ mm, $D_{SD} = 80$ mm, and (c) $d = 1.50$ mm, $t = 20.0$ mm, $D_{SD} = 80$ mm.

CRediT authorship contribution statement

Zebin Lin: Conceptualization, Methodology, Formal analysis, Software, Writing – original draft, Writing – review & editing. **Ziwen Pan:** Conceptualization, Methodology, Formal analysis, Writing – original draft, Writing – review & editing, Funding acquisition. **Zhe Wang:** Software. **Zhengyang He:** Software. **Jingyu Dong:** Software, Writing – review & editing. **Jiandang Liu:** Software, Writing – review & editing. **Hongjun Zhang:** Software, Writing – review & editing. **Bangjiao Ye:** Project administration, Funding acquisition.

Declaration of competing interest

The authors declare that they have no known competing financial interests or personal relationships that could have appeared to influence the work reported in this paper.

Acknowledgments

This work was financially supported by the National Natural Science Foundation of China (Grant No. 12005221).

References

[1] M. Aramini, C. Milanese, A.D. Hillier, A. Girella, C. Horstmann, T. Klassen, K. Ishida, M. Dornheim, C. Pistidda, Using the emission of muonic X-rays as a spectroscopic tool for the investigation of the local chemistry of elements, Nanomaterials 10 (7) (2020) 1260, http://dx.doi.org/10.3390/nano10071260.

[2] A. Hillier, D.M. Paul, K. Ishida, Probing beneath the surface without a scratch-Bulk non-destructive elemental analysis using negative muons, Microchem. J. 125 (2016) 203–207, http://dx.doi.org/10.1016/j.microc.2015.11.031.

[3] K. Ninomiya, T. Nagatomo, K. Kubo, P. Strasser, N. Kawamura, K. Shimomura, Y. Miyake, T. Saito, W. Higemoto, Development of elemental analysis by muonic X-ray measurement in J-PARC, in: J. Phys.: Conf. Ser., 225, (1) IOP Publishing, 2010, 012040, http://dx.doi.org/10.1088/1742-6596/225/1/012040.

[4] M. Clemenza, M. Bonesini, M. Carpinelli, O. Cremonesi, E. Fiorini, G. Gorini, A. Hillier, K. Ishida, A. Menegolli, E. Mocchiutti, et al., Muonic atom X-ray spectroscopy for non-destructive analysis of archeological samples, J. Radioanal. Nucl. Chem. 322 (3) (2019) 1357–1363, http://dx.doi.org/10.1007/s10967-019-06927-6.

[5] H. Daniel, Application of muonic X-rays for elemental analysis, Biol. Trace Elem. Res. 13 (1) (1987) 301–318, http://dx.doi.org/10.1007/BF02796642.

[6] K. Terada, A. Sato, K. Ninomiya, Y. Kawashima, K. Shimomura, G. Yoshida, Y. Kawai, T. Osawa, S. Tachibana, Non-destructive elemental analysis of a carbonaceous chondrite with direct current Muon beam at MuSIC, Sci. Rep. 7 (1) (2017) 1–6, http://dx.doi.org/10.1038/s41598-017-15719-5.

[7] I. Umegaki, Y. Higuchi, Y. Kondo, K. Ninomiya, S. Takeshita, M. Tampo, H. Nakano, H. Oka, J. Sugiyama, M.K. Kubo, et al., Nondestructive high-sensitivity detections of metallic lithium deposited on a battery anode using muonic X-rays, Anal. Chem. 92 (12) (2020) 8194–8200, http://dx.doi.org/10.1021/acs.analchem.0c00370.

[8] K. Shimada-Takaura, K. Ninomiya, A. Sato, N. Ueda, M. Tampo, S. Takeshita, I. Umegaki, Y. Miyake, K. Takahashi, A novel challenge of nondestructive analysis on OGATA Koan's sealed medicine by muonic X-ray analysis, J. Nat. Med. 75 (3) (2021) 532–539, http://dx.doi.org/10.1007/s11418-021-01487-0.

[9] A. Hillier, K. Ishida, P. Seller, M.C. Veale, M.D. Wilson, Element specific imaging using muonic X-rays, in: Proceedings of the 14th International Conference on Muon Spin Rotation, Relaxation and Resonance (μSR2017), 2018, 011042, http://dx.doi.org/10.7566/JPSCP.21.011042.

[10] M. Katsuragawa, M. Tampo, K. Hamada, A. Harayama, Y. Miyake, S. Oshita, G. Sato, T. Takahashi, S. Takeda, S. Watanabe, et al., A compact imaging system with a CdTe double-sided strip detector for non-destructive analysis using negative muonic X-rays, Nucl. Instrum. Methods Phys. Res. A 912 (2018) 140–143, http://dx.doi.org/10.1016/j.nima.2017.11.004.

[11] G. Eaton, The ISIS pulsed muon facility, Z. Phys. C 56 (1) (1992) S232–S239, http://dx.doi.org/10.1007/bf02426802.

[12] Y. Miyake, K. Nishiyama, N. Kawamura, P. Strasser, S. Makimura, A. Koda, K. Shimomura, H. Fujimori, K. Nakahara, R. Kadono, et al., J-PARC muon source, MUSE, Nucl. Instrum. Methods Phys. Res. A 600 (1) (2009) 22–24, http://dx.doi.org/10.1016/j.nima.2008.11.016.

[13] J.a. Braga, Coded aperture imaging in high-energy astrophysics, Publ. Astron. Soc. Pac. 132 (1007) (2019) 012001, http://dx.doi.org/10.1088/1538-3873/ab450a.

[14] R. Accorsi, F. Gasparini, R.C. Lanza, Optimal coded aperture patterns for improved SNR in nuclear medicine imaging, Nucl. Instrum. Methods Phys. Res. A 474 (3) (2001) 273–284, http://dx.doi.org/10.1016/S0168-9002(01)01326-2.

[15] M. Gmar, M. Agelou, F. Carrel, V. Schoepff, GAMPIX: A new generation of gamma camera, Nucl. Instrum. Methods Phys. Res. A 652 (1) (2011) 638–640, http://dx.doi.org/10.1016/j.nima.2010.09.003.

[16] A. Haboub, A. MacDowell, S. Marchesini, D. Parkinson, Coded Aperture Imaging for Fluorescent X-rays-Biomedical Applications, Tech. rep., Lawrence Berkeley National Lab. (LBNL), Berkeley, CA (United States), 2013.

[17] S. Agostinelli, J. Allison, K.a. Amako, J. Apostolakis, H. Araujo, P. Arce, M. Asai, D. Axen, S. Banerjee, G. Barrand, et al., GEANT4—A simulation toolkit, Nucl. Instrum. Methods Phys. Res. A 506 (3) (2003) 250–303, http://dx.doi.org/10.1016/S0168-9002(03)01368-8.

[18] J. Allison, K. Amako, J. Apostolakis, H. Araujo, P.A. Dubois, M. Asai, G. Barrand, R. Capra, S. Chauvie, R. Chytracek, et al., Geant4 developments and applications, IEEE Trans. Nucl. Sci. 53 (1) (2006) 270–278, http://dx.doi.org/10.1109/TNS.2006.869826.

[19] J. Allison, K. Amako, J. Apostolakis, P. Arce, M. Asai, T. Aso, E. Bagli, A. Bagulya, S. Banerjee, G. Barrand, et al., Recent developments in Geant4, Nucl. Instrum. Methods Phys. Res. A 835 (2016) 186–225, http://dx.doi.org/10.1016/j.nima.2016.06.125.

[20] E.E. Fenimore, T.M. Cannon, Coded aperture imaging with uniformly redundant arrays, Appl. Opt. 17 (3) (1978) 337–347, http://dx.doi.org/10.1364/AO.17.000337.

[21] E. Fenimore, Coded aperture imaging: the modulation transfer function for uniformly redundant arrays, Appl. Opt. 19 (14) (1980) 2465–2471, http://dx.doi.org/10.1364/AO.19.002465.

[22] R. Zhang, P. Gong, X. Tang, P. Wang, C. Zhou, X. Zhu, L. Gao, D. Liang, Z. Wang, Reconstruction method for gamma-ray coded-aperture imaging based on convolutional neural network, Nucl. Instrum. Methods Phys. Res. A 934 (2019) 41–51, http://dx.doi.org/10.1016/j.nima.2019.04.055.

[23] A. Kulow, A.G. Buzanich, U. Reinholz, F. Emmerling, S. Hampel, U.E.A. Fittschen, C. Streli, M. Radtke, Comparison of three reconstruction methods based on deconvolution, iterative algorithm and neural network for X-ray fluorescence imaging with coded aperture optics, J. Anal. At. Spectrom. 35 (7) (2020) 1423–1434, http://dx.doi.org/10.1039/D0JA00146E.

[24] F.J.B. Roselló, F.S. Martıńez, V.R. Velasco, The EM imaging reconstruction method in γ-ray astronomy, Nucl. Instrum. Methods Phys. Res. B 145 (3) (1998) 469–481, http://dx.doi.org/10.1016/S0168-583X(98)00513-8.

[25] L.A. Shepp, Y. Vardi, Maximum likelihood reconstruction for emission tomography, IEEE Trans. Med. Imaging 1 (2) (1982) 113–122, http://dx.doi.org/10.1109/TMI.1982.4307558.

[26] G. Daniel, O. Limousin, Extended sources reconstructions by means of coded mask aperture systems and deep learning algorithm, Nucl. Instrum. Methods Phys. Res. A 1012 (2021) 165600, http://dx.doi.org/10.1016/j.nima.2021.165600.

[27] E. Fenimore, T. Cannon, Uniformly redundant arrays: digital reconstruction methods, Appl. Opt. 20 (10) (1981) 1858–1864, http://dx.doi.org/10.1364/AO.20.001858.

[28] G. Sato, K. Hagino, S. Watanabe, K. Genba, A. Harayama, H. Kanematsu, J. Kataoka, M. Katsuragawa, M. Kawaharada, S. Kobayashi, et al., The Si/CdTe semiconductor camera of the ASTRO-H hard X-ray imager (HXI), Nucl. Instrum. Methods Phys. Res. A 831 (2016) 235–241, http://dx.doi.org/10.1016/j.nima.2016.03.038.

[29] K. Hagino, H. Odaka, G. Sato, S. Watanabe, S. Takeda, M. Kokubun, T. Fukuyama, S. Saito, T. Sato, Y. Ichinohe, et al., Imaging and spectral performance of CdTe double-sided strip detectors for the Hard X-ray imager onboard ASTRO-H, in: Space Telescopes and Instrumentation 2012: Ultraviolet To Gamma Ray, vol. 8443, SPIE, 2012, pp. 1484–1494, http://dx.doi.org/10.1117/12.926052.

[30] S.R. Gottesman, E.E. Fenimore, New family of binary arrays for coded aperture imaging, Appl. Opt. 28 (20) (1989) 4344–4352, http://dx.doi.org/10.1364/AO.28.004344.

[31] P. Seller, S. Bell, R.J. Cernik, C. Christodoulou, C. Egan, J. Gaskin, S. Jacques, S. Pani, B. Ramsey, C. Reid, et al., Pixellated Cd (Zn) Te high-energy X-ray instrument, J. Instrum. 6 (12) (2011) C12009, http://dx.doi.org/10.1088/1748-0221/6/12/c12009.

[32] Z. Wang, A.C. Bovik, A universal image quality index, IEEE Signal Process. Lett. 9 (3) (2002) 81–84, http://dx.doi.org/10.1109/97.995823.

[33] R. Accorsi, R.C. Lanza, Near-field artifact reduction in planar coded aperture imaging, Appl. Opt. 40 (26) (2001) 4697–4705, http://dx.doi.org/10.1364/AO.40.004697.

[34] T. Lee, W. Lee, High performance γ-ray imager using dual anti-mask method for the investigation of high-energy nuclear materials, Nucl. Eng. Technol. 53 (7) (2021) 2371–2376, http://dx.doi.org/10.1016/j.net.2021.01.027.